

Benchmarking Quantum Simulators

Andrew Shaw^{1,*}

¹University of Maryland, College Park, MD 20742, USA

(Dated: October 26, 2021)

Time-Averaged Mixed-state Equivalence (TAME) is used to benchmark quantum simulators with classical computing resources. The classical computation is feasible even if direct computation of the real-time dynamics is prohibitively costly.

I. TIME-AVERAGED MIXED-STATE EQUIVALENCE

Time-Averaged Mixed-state Equivalence (TAME) relates the real-time dynamics of *pure quantum states* and the expectation values of *mixed quantum states*.

A. Time-Averaged Dynamics

An observable \hat{O} undergoes time evolution governed by a Hamiltonian \hat{H} :

$$\hat{H} = \sum_{\alpha} \mathcal{E}_{\alpha} |\alpha\rangle\langle\alpha|, \quad (\text{I.1})$$

$$\hat{O} = \sum_{\alpha,\beta} \mathcal{O}_{\alpha,\beta} |\alpha\rangle\langle\beta| \quad (\text{I.2})$$

The real-time dynamics of \hat{O} are as follows [1]:

$$\hat{O}(t) = e^{i\hat{H}t} \hat{O} e^{-i\hat{H}t} \quad (\text{I.3})$$

$$\hat{O}(t) = \sum_{\alpha,\beta} \mathcal{O}_{\alpha,\beta} e^{-it(\mathcal{E}_{\beta} - \mathcal{E}_{\alpha})} |\alpha\rangle\langle\beta| \quad (\text{I.4})$$

The *time-averaged observable* is the following:

$$\hat{\Omega} = \lim_{t \rightarrow \infty} \frac{1}{t} \int_0^t dt' \hat{O}(t') \quad (\text{I.5})$$

$$\hat{\Omega} = \sum_{\alpha} \mathcal{O}_{\alpha,\alpha} |\alpha\rangle\langle\alpha| \quad (\text{I.6})$$

The *time-averaged expectation value* of a pure state $|\psi\rangle$ is the following:

$$\langle\psi|\hat{\Omega}|\psi\rangle = \sum_{\alpha} |c_{\alpha}|^2 \mathcal{O}_{\alpha,\alpha} \quad (\text{I.7})$$

$$|\psi\rangle = \sum_{\alpha} c_{\alpha} |\alpha\rangle \quad (\text{I.8})$$

B. Mixed State Expectation Values

A mixed quantum state is composed of an ensemble of pure states $|\psi_k\rangle$, with observational probabilities p_k . Its *density matrix* [2, 3] is the following:

$$\rho = \sum_k p_k |\psi_k\rangle\langle\psi_k|, \quad (\text{I.9})$$

$$= \sum_{\alpha,\beta} \mathcal{P}_{\alpha,\beta} |\alpha\rangle\langle\beta| \quad (\text{I.10})$$

The expectation value of \hat{O} is as follows:

$$\langle\hat{O}\rangle = \text{Tr}[\rho\hat{O}] \quad (\text{I.11})$$

$$\langle\hat{O}\rangle = \sum_{\alpha,\beta} \mathcal{P}_{\alpha,\beta} \mathcal{O}_{\beta,\alpha} \quad (\text{I.12})$$

Orthodox mixed states commute with the Hamiltonian:

$$[\tilde{\rho}, \hat{H}] = 0 \quad (\text{I.13})$$

$$\tilde{\rho} = \sum_{\alpha} \tilde{\mathcal{P}}_{\alpha} |\alpha\rangle\langle\alpha| \quad (\text{I.14})$$

The *orthodox expectation value* is the following:

$$\text{Tr}[\tilde{\rho}\hat{O}] = \sum_{\alpha} \tilde{\mathcal{P}}_{\alpha} \mathcal{O}_{\alpha,\alpha} \quad (\text{I.15})$$

Density matrices must be *positive semi-definite* with $\text{Tr}(\rho) = 1$ [4], which requires the following conditions to be satisfied:

$$\sum_{\alpha} \tilde{\mathcal{P}}_{\alpha} = 1, \quad \tilde{\mathcal{P}}_{\alpha} \in \mathbb{R}^+ \quad (\text{I.16})$$

The time-averaged expectation values of each pure state are equivalent to the expectation values of an orthodox mixed state. This mapping is not one-to-one, as a continuum of pure states share a corresponding orthodox mixed state (Figure 1).

C. Coarse-Grained TAME

TAME is coarse-grained by integrating over the pure states and the orthodox mixed states [5–8].

* Electronic Address: ashaw12@umd.edu

The *coarse-grained time-averaged expectation value* is obtained by integrating over all pure states:

$$\langle \hat{\Omega} \rangle_c = \int d\psi \langle \psi | \hat{\Omega} | \psi \rangle \quad (\text{I.17})$$

$$= \int d\psi \sum_{\alpha} |c_{\alpha}(\psi)|^2 \mathcal{O}_{\alpha,\alpha} \quad (\text{I.18})$$

$$= \sum_{\alpha} \mathcal{O}_{\alpha,\alpha} \int d\psi |c_{\alpha}(\psi)|^2 \quad (\text{I.19})$$

$$= \text{Tr}[\hat{O}] \cdot \frac{1}{\dim\{\hat{H}\}} \quad (\text{I.20})$$

The *coarse-grained orthodox expectation value* is obtained by integrating over all orthodox mixed states:

$$\langle \hat{O} \rangle_c = \int d\tilde{\rho} \text{Tr}[\tilde{\rho} \hat{O}] \quad (\text{I.21})$$

$$= \int d\tilde{\rho} \sum_{\alpha} \tilde{\mathcal{P}}_{\alpha} \mathcal{O}_{\alpha,\alpha} \quad (\text{I.21})$$

$$= \sum_{\alpha} \mathcal{O}_{\alpha,\alpha} \int d\tilde{\rho} \tilde{\mathcal{P}}_{\alpha} \quad (\text{I.22})$$

$$= \text{Tr}[\hat{O}] \cdot \frac{1}{\dim\{\hat{H}\}} \quad (\text{I.23})$$

Integrating over the pure states and the orthodox mixed states yields an identical quantity.

II. QUANTUM SIMULATION BENCHMARK

Benchmarking the output of a *quantum simulator* [9, 10] can be accomplished with TAME. This requires determining the expectation values of orthodox mixed states using *classical computing resources* [11].

A. Orthodox Mixed State Computation

Orthodox mixed states can be expressed by applying positive-real functions $f(x)$ to the Hamiltonian:

$$\tilde{\rho}(f) = \frac{f(\hat{H})}{\text{Tr}[f(\hat{H})]} \quad (\text{II.1})$$

$$= \frac{1}{Z} f(\hat{H}) \quad (\text{II.2})$$

A positive-real function can be expressed as follows:

$$f(x) = \int_{-\infty}^{\infty} dt \delta(x-t) f(t) \quad (\text{II.3})$$

$$= \lim_{\sigma \rightarrow 0} \frac{1}{|\sigma| \sqrt{\pi}} \int_{-\infty}^{\infty} dt e^{-\left(\frac{x-t}{\sigma}\right)^2} f(t) \quad (\text{II.4})$$

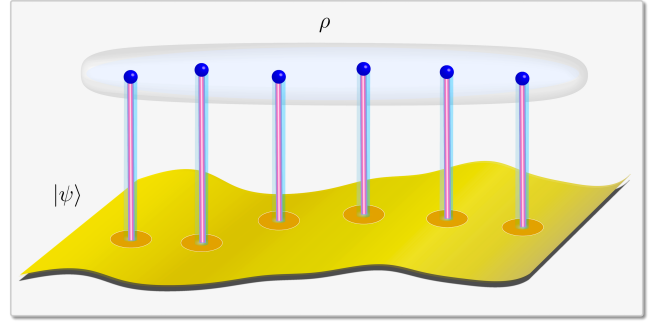


FIG. 1. [Upper Panel]: Orthodox mixed states (blue) reside in the space of mixed states (gray). [Lower Panel]: TAME relates each orthodox mixed state to a subset of states (golden) in the space of pure states (yellow).

A general orthodox mixed state can be expressed as follows:

$$\tilde{\rho}(f) = \frac{1}{Z} \left[\lim_{\sigma \rightarrow 0} \frac{1}{|\sigma| \sqrt{\pi}} \int_{-\infty}^{\infty} dt e^{-\left(\frac{\hat{H}-t}{\sigma}\right)^2} f(t) \right] \quad (\text{II.5})$$

As such, it is sufficient to consider *gaussian orthodox mixed states*:

$$\tilde{\rho}_g(\epsilon, \sigma) = \frac{1}{Z} e^{-\left(\frac{\hat{H}-\epsilon}{\sigma}\right)^2} \quad (\text{II.6})$$

These can be re-expressed in terms of a Hermitian operator \hat{K} and a real parameter τ :

$$\tilde{\rho}_g(\epsilon, \sigma) = \frac{1}{Z} e^{-\hat{K}\tau} \quad (\text{II.7})$$

The expectation value of \hat{O} is as follows:

$$\langle \hat{O} \rangle = \frac{1}{Z} \text{Tr} \left[e^{-\hat{K}\tau} \hat{O} \right] \quad (\text{II.8})$$

$$= \frac{1}{Z} \sum_a \langle a | e^{-\hat{K}\tau} \hat{O} | a \rangle \quad (\text{II.9})$$

The expectation value can be classically computed in a manner similar to the *path integral* [12]. This is accomplished by discretizing $e^{-\hat{K}\tau}$:

$$e^{-\hat{K}\tau} \rightarrow e^{-\hat{K}\Delta} e^{-\hat{K}\Delta} \dots e^{-\hat{K}\Delta} \quad (\text{II.10})$$

The identity is inserted between the matrix exponentials:

$$e^{-\hat{K}\tau} = \sum_{a_1} \dots \sum_{a_N} |a_1\rangle \langle a_1| e^{-\hat{K}\Delta} |a_2\rangle \langle a_2| e^{-\hat{K}\Delta} |a_3\rangle \langle a_3| \dots |a_{N-1}\rangle \langle a_{N-1}| e^{-\hat{K}\Delta} |a_N\rangle \langle a_N| \quad (\text{II.11})$$

This can be re-expressed as a sum over *configurations* $\vec{a} = \{a_1, \dots, a_N\}$:

$$e^{-\hat{K}\tau} = \sum_{\vec{a}} S(\vec{a}) |a_1\rangle \langle a_N| \quad (\text{II.12})$$

$$S(\vec{a}) = \langle a_1 | e^{-\hat{K}\Delta} | a_2 \rangle \dots \langle a_{N-1} | e^{-\hat{K}\Delta} | a_N \rangle \quad (\text{II.13})$$

The expectation value of \hat{O} is the following:

$$\langle \hat{O} \rangle = \frac{1}{\mathcal{Z}} \sum_a \left[\sum_{\vec{a}} \langle a | S(\vec{a}) | a_1 \rangle \langle a_N | \hat{O} | a \rangle \right] \quad (\text{II.14})$$

$$= \frac{1}{\mathcal{Z}} \sum_{\vec{a}} S(\vec{a}) \langle a_N | \hat{O} | a_1 \rangle \quad (\text{II.15})$$

$$= \frac{1}{\mathcal{Z}} \sum_{\vec{a}} |S(\vec{a})| O(\vec{a}) \quad (\text{II.16})$$

Classical computing resources can be used to sample from the configurations with the following probability:¹

$$P(\vec{a}_{\text{samp}} \in \vec{a}_j) = \frac{1}{\xi} \frac{|S(\vec{a}_j)|}{\mathcal{Z}} \quad (\text{II.17})$$

The sampled configurations can be used to estimate $\langle \hat{O} \rangle$ as follows:

$$\langle \hat{O} \rangle \approx \frac{\xi}{N_{\text{samp}}} \sum_{k=1}^{N_{\text{samp}}} O(\vec{a}_{\text{samp}}^{(k)}) \quad (\text{II.18})$$

B. Direct Benchmark

Classical computing resources can be used to compute the orthodox expectation value of $\tilde{\rho}(f)$:

$$\tilde{\rho}(f) = \frac{1}{\mathcal{Z}} f(\hat{H}) \quad (\text{II.19})$$

$$= \frac{1}{\mathcal{Z}} \sum_{\alpha} f(\mathcal{E}_{\alpha}) |\alpha\rangle \langle \alpha| \quad (\text{II.20})$$

The corresponding *direct benchmarking states* take the following form:

$$|\psi(f)\rangle = \sum_{\alpha} e^{i\phi_{\alpha}} \sqrt{\frac{f(\mathcal{E}_{\alpha})}{\mathcal{Z}}} |\alpha\rangle \quad (\text{II.21})$$

The direct benchmarking states satisfy the following property:

$$\langle \psi(f) | \hat{\Omega} | \psi(f) \rangle = \text{Tr} \left[\tilde{\rho}(f) \hat{O} \right] \quad (\text{II.22})$$

A quantum simulator generates dynamics governed by the *simulation Hamiltonian* \hat{H}_s :

$$\hat{H}_s = \sum_{\alpha^s} \mathcal{E}_{\alpha^s} |\alpha^s\rangle \langle \alpha^s| \quad (\text{II.23})$$

The quantum simulator provides access to the *simulated observable*:

$$\hat{O}_s(t) = e^{i\hat{H}_s t} \hat{O} e^{-i\hat{H}_s t} \quad (\text{II.24})$$

The *simulated time-averaged observable* is as follows:

$$\hat{\Omega}_s = \lim_{t \rightarrow \infty} \frac{1}{t} \int_0^t dt' \hat{O}_s(t') \quad (\text{II.25})$$

If the quantum simulator exactly reproduces the target dynamics, the *simulated time-averaged expectation value* will recover the orthodox expectation value for all direct benchmarking states:

$$\lim_{\hat{H}_s \rightarrow \hat{H}} \langle \psi(f) | \hat{\Omega}_s | \psi(f) \rangle = \text{Tr} \left[\tilde{\rho}(f) \hat{O} \right], \quad \forall |\psi(f)\rangle \quad (\text{II.26})$$

C. Coarse-Grained Benchmark

An analogous procedure can be performed by coarse-graining TAME over a portion of the Hilbert space.

1. Projecting Coarse-Grained TAME

The Hamiltonian can be written in the following form:

$$\hat{H} = \hat{H}_P \oplus \hat{H}_Q \quad (\text{II.27})$$

The Hilbert space of \hat{H} can be expressed as follows:

$$\mathcal{H} = \mathcal{H}_P \oplus \mathcal{H}_Q \quad (\text{II.28})$$

The Hilbert subspace \mathcal{H}_Q is spanned by the states $|Q_i\rangle$:

$$\mathcal{H}_Q = \overline{\text{span}} \{ |Q_1\rangle, |Q_2\rangle, \dots \} \quad (\text{II.29})$$

The *projection operator* [13] onto \mathcal{H}_P is the following:

$$\hat{P} = \hat{\mathbb{1}} - \sum_i |Q_i\rangle \langle Q_i| \quad (\text{II.30})$$

To coarse-grain TAME on \mathcal{H}_P , pure states and orthodox mixed states with support on \mathcal{H}_Q are excluded from the integral.

¹ Monte-Carlo techniques can be used to sample from a target probability distribution (Appendix).

To enforce this exclusion, the integral over pure states is modified as follows:

$$\int d\psi \rightarrow \int d\psi \mathcal{J}(\hat{P}, \psi) \quad (\text{II.31})$$

$$\mathcal{J}(\hat{P}, \psi) = \delta\{1 - \langle \psi | \hat{P} | \psi \rangle\} \quad (\text{II.32})$$

Likewise, the integral over orthodox mixed states is modified as follows:

$$\int d\tilde{\rho} \rightarrow \int d\tilde{\rho} \mathcal{R}(\hat{P}, \tilde{\rho}) \quad (\text{II.33})$$

$$\mathcal{R}(\hat{P}, \tilde{\rho}) = \delta\{1 - \text{Tr}[\hat{P} \tilde{\rho}]\} \quad (\text{II.34})$$

The *projected coarse-grained time-averaged expectation value* is the following:

$$\langle \hat{\Omega} \rangle_{c,P} = \int d\psi \mathcal{J}(\hat{P}, \psi) \langle \psi | \hat{\Omega} | \psi \rangle \quad (\text{II.35})$$

$$= \text{Tr}[\hat{P} \hat{\Omega}] \cdot \frac{1}{\dim\{\hat{H}_P\}} \quad (\text{II.36})$$

The *projected coarse-grained orthodox expectation value* is the following:

$$\langle \hat{O} \rangle_{c,P} = \int d\tilde{\rho} \mathcal{R}(\hat{P}, \tilde{\rho}) \text{Tr}[\tilde{\rho} \hat{O}] \quad (\text{II.37})$$

$$= \text{Tr}[\hat{P} \hat{O}] \cdot \frac{1}{\dim\{\hat{H}_P\}} \quad (\text{II.38})$$

Integrating over compatible subsets of the pure states and orthodox mixed states yields an identical quantity.

2. Simulation Benchmark

A *subspace mapping* \mathcal{L} uses a Hamiltonian to specify a Hilbert subspace \mathcal{H}_P with projection operator \hat{P} :

$$\mathcal{L}(\hat{H}) = \mathcal{H}_P \quad (\text{II.39})$$

$$[\hat{P}, \hat{H}] = 0 \quad (\text{II.40})$$

Benchmark orthodox mixed states $\tilde{\rho}_b$ have support solely on \mathcal{H}_P :

$$\tilde{\rho}_b \in \{\mathcal{H} \otimes \mathcal{H}^*\}_P, \forall \tilde{\rho}_b \quad (\text{II.41})$$

The projected coarse-grained orthodox expectation value is approximated by sampling from the benchmark orthodox mixed states with a uniform probability:

$$\langle \hat{O} \rangle_{c,P} \approx \frac{1}{N_{\text{samp}}} \sum_{i=1}^{N_{\text{samp}}} \text{Tr}[\tilde{\rho}_b^{(i)} \hat{O}] \quad (\text{II.42})$$

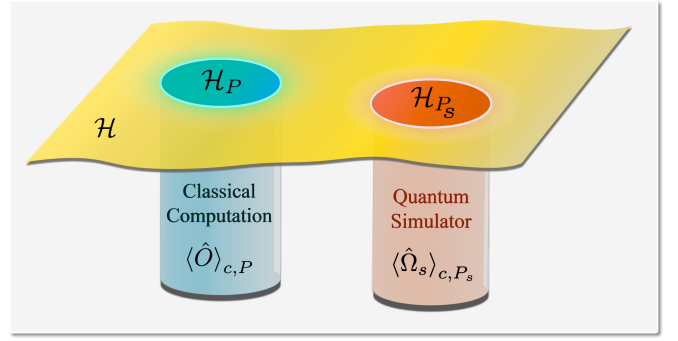


FIG. 2. [Upper Panel]: \mathcal{H}_P (blue) and \mathcal{H}_{P_s} (orange) are subspaces of \mathcal{H} (yellow) that are specified by \hat{H} and \hat{H}_s . [Lower Panel]: Classical computation and quantum simulation are used to probe the equivalence of \mathcal{H}_P and \mathcal{H}_{P_s} .

The subspace mapping is applied to the simulation Hamiltonian to specify a Hilbert subspace \mathcal{H}_{P_s} with projection operator \hat{P}_s :

$$\mathcal{L}(\hat{H}_s) = \mathcal{H}_{P_s} \quad (\text{II.43})$$

$$[\hat{P}_s, \hat{H}_s] = 0 \quad (\text{II.44})$$

Coarse-grained benchmarking states $|\psi_b\rangle$ have support solely on \mathcal{H}_{P_s} :

$$|\psi_b\rangle \in \mathcal{H}_{P_s}, \forall |\psi_b\rangle \quad (\text{II.45})$$

The quantum simulator can be used to approximate the *projected coarse-grained simulated time-averaged expectation value*:

$$\langle \hat{\Omega}_s \rangle_{c,P_s} = \int d\psi \mathcal{J}(\hat{P}_s, \psi) \langle \psi | \hat{\Omega}_s | \psi \rangle \quad (\text{II.46})$$

This is accomplished by sampling from the coarse-grained benchmarking states with a uniform probability:

$$\langle \hat{\Omega}_s \rangle_{c,P_s} \approx \frac{1}{N_{\text{samp}}} \sum_{i=1}^{N_{\text{samp}}} \langle \psi_b^{(i)} | \hat{\Omega}_s | \psi_b^{(i)} \rangle \quad (\text{II.47})$$

If $\mathcal{H}_P = \mathcal{H}_{P_s}$, the projected coarse-grained orthodox expectation value will equal the projected coarse-grained simulated time-averaged expectation value (Figure 2).

III. ENERGY-WINDOW TIME-AVERAGING

Energy-window Time-Averaging (ETA) is a coarse-grained benchmarking procedure. Coarse-grained benchmarking can be represented schematically in three stages:

I. Projection: Establish a subspace mapping.

II. Standardization: Sample benchmark orthodox mixed states to establish a *standard of comparison*.

III. Arbitration: Sample coarse-grained benchmarking states to establish a *simulation diagnostic*.

A. Projection

Both ETA-Variant I and ETA-Variant II require an *energy-window* Δ_ϵ to perform projection:

$$\epsilon_{\min} < \mathcal{E} < \epsilon_{\max}, \quad \forall \mathcal{E} \in \Delta_\epsilon \quad (\text{III.1})$$

1. Variant I

In ETA-Variant I, the subspace mapping uses the expectation value of the Hamiltonian to define a subset $\mathcal{H}_P^{(I)} \in \mathcal{H}$. States with average energies that fall within the energy-window are members of the subset (Figure 3):

$$\langle \psi | \hat{H} | \psi \rangle \in \Delta_\epsilon, \quad \forall |\psi\rangle \in \mathcal{H}_P^{(I)} \quad (\text{III.2})$$

2. Variant II

In ETA-Variant II, the subspace mapping uses the eigenstates of the Hamiltonian to define a subspace $\mathcal{H}_P^{(II)} \in \mathcal{H}$. States with eigenvalues inside the energy-window are members of the subspace (Figure 4):

$$\hat{H} |\alpha_i\rangle = \mathcal{E}_{\alpha_i} |\alpha_i\rangle, \quad \mathcal{E}_{\alpha_i} \in \Delta_\epsilon \quad (\text{III.3})$$

$$\mathcal{H}_P^{(II)} = \overline{\text{span}}\{ |\alpha_1\rangle, |\alpha_2\rangle, \dots \} \quad (\text{III.4})$$

3. Energy-Window Selection

To select an energy-window, the *extremum energy eigenvalues* must be determined. The *extremizing orthodox mixed state* is the following:

$$\tilde{\rho}_{\text{ext}}^{(\tau)} = \frac{1}{Z} e^{\hat{H}\tau} \quad (\text{III.5})$$

Taking $\tau \rightarrow -\infty$ results in the *minimum energy*:

$$\lim_{\tau \rightarrow -\infty} \text{Tr} \left[\tilde{\rho}_{\text{ext}}^{(\tau)} \hat{H} \right] = \mathcal{E}_{\min} \quad (\text{III.6})$$

Taking $\tau \rightarrow \infty$ results in the *maximum energy*:

$$\lim_{\tau \rightarrow \infty} \text{Tr} \left[\tilde{\rho}_{\text{ext}}^{(\tau)} \hat{H} \right] = \mathcal{E}_{\max} \quad (\text{III.7})$$

Viable energy-windows have the following restriction:

$$\mathcal{E}_{\min} < \epsilon_{\min} < \epsilon_{\max} < \mathcal{E}_{\max} \quad (\text{III.8})$$

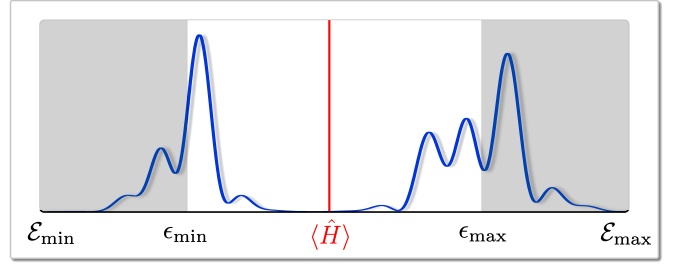


FIG. 3. The energy-eigenstate decomposition (blue) of a state in the ETA-Variant I subset, has an average energy (red) that falls within the energy-window (white).

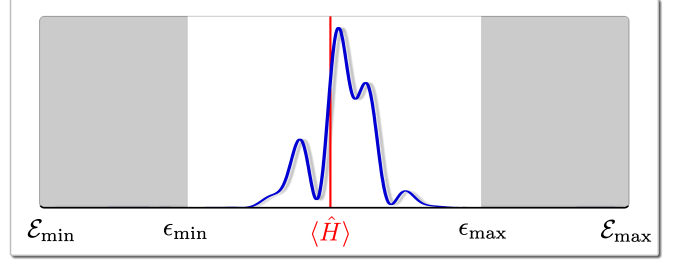


FIG. 4. The energy-eigenstate decomposition (blue) of a state in the ETA-Variant II subspace, is zero outside of the energy-window (white).

B. Standardization

In ETA-Variant I and ETA-Variant II, benchmark orthodox mixed states are generated to establish a standard of comparison.

1. Variant I

In ETA-Variant I, orthodox mixed states are generated pseudo-randomly using positive-real functions $f_\gamma(x)$.

These functions are normalized over the extremum eigenvalues:

$$\int_{\mathcal{E}_{\min}}^{\mathcal{E}_{\max}} d\mathcal{E} f_\gamma(\mathcal{E}) = 1 \quad (\text{III.9})$$

The average energy of the functions lies within the energy window:

$$\int_{\mathcal{E}_{\min}}^{\mathcal{E}_{\max}} d\mathcal{E} f_\gamma(\mathcal{E}) \mathcal{E} \in \Delta_\epsilon \quad (\text{III.10})$$

An orthodox mixed state is constructed from a chosen function $f_{\gamma'}(x)$. If $\langle \hat{H} \rangle$ falls within the energy-window, a benchmark orthodox mixed state was generated:

$$\begin{aligned} \langle \hat{H} \rangle &\in \Delta_\epsilon, \\ \tilde{\rho}(f_{\gamma'}) &\in \left\{ \mathcal{H} \otimes \mathcal{H}^* \right\}_P^{(I)} \end{aligned} \quad (\text{III.11})$$

2. Variant II

In ETA-Variant II, gaussian orthodox mixed states are generated pseudo-randomly:

$$\tilde{\rho}_g(\epsilon, \sigma) = \frac{1}{\mathcal{Z}} \sum_{\alpha} e^{-\left(\frac{\mathcal{E}_{\alpha} - \epsilon}{\sigma}\right)^2} |\alpha\rangle\langle\alpha| \quad (\text{III.12})$$

To increase the likelihood that a benchmark orthodox mixed state is generated, ϵ and σ are constrained:

$$\epsilon \in \Delta_{\epsilon} \quad (\text{III.13})$$

$$e^{-\left(\frac{\epsilon_{\min} - \epsilon}{\sigma}\right)^2} \ll 1 \quad (\text{III.14})$$

$$e^{-\left(\frac{\epsilon_{\max} - \epsilon}{\sigma}\right)^2} \ll 1 \quad (\text{III.15})$$

A gaussian orthodox mixed state is constructed from the chosen parameters (ϵ, σ) . The expectation value of the Hamiltonian and its variance are determined:

$$\text{Var}(\hat{H}) = \langle \hat{H}^2 \rangle - \langle \hat{H} \rangle^2 \quad (\text{III.16})$$

If $\langle \hat{H} \rangle$ and its uncertainty fall outside the energy-window, a benchmark orthodox mixed state was not generated:

$$\langle \hat{H} \rangle \pm \sqrt{\text{Var}(\hat{H})} \notin \Delta_{\epsilon},$$

$$\tilde{\rho}_g(\epsilon, \sigma) \notin \left\{ \mathcal{H} \otimes \mathcal{H}^* \right\}_P^{(II)} \quad (\text{III.17})$$

C. Arbitration

In ETA-Variant I and ETA-Variant II, coarse-grained benchmarking states are prepared to establish a simulation diagnostic.

1. State Preparation

a. Variant I

In ETA-Variant I, coarse-grained benchmarking states are prepared using a *variational hybrid quantum-classical algorithm* [14]. These algorithms seek to use classical optimization to prepare pure states that minimize a *cost-function* [15].

A set of pure states is identified by applying a class of unitary transformations to an *edge state* $|\psi_e\rangle$:

$$|\psi_e^{(\vec{p})}\rangle = \hat{U}^{(\vec{p})} |\psi_e\rangle \quad (\text{III.18})$$

The cost-function is the absolute difference between the expectation value of the simulation Hamiltonian and the center of the energy-window:

$$\mathcal{C}_e(\vec{p}) = \left| \left\langle \psi_e^{(\vec{p})} \right| \hat{H}_s \left| \psi_e^{(\vec{p})} \right\rangle - \left(\frac{\epsilon_{\max} + \epsilon_{\min}}{2} \right) \right| \quad (\text{III.19})$$

An edge state is generated pseudo-randomly, and the variational hybrid quantum-classical algorithm is allowed to run to completion. During the course of the algorithm, coarse-grained benchmarking states may be generated.

The accessible coarse-grained benchmarking states are identified by the parameters (e, \vec{p}_b) for which the following condition holds:

$$\left\langle \psi_e^{(\vec{p}_b)} \right| \hat{H}_s \left| \psi_e^{(\vec{p}_b)} \right\rangle \in \Delta_{\epsilon}, \quad \forall \left| \psi_e^{(\vec{p}_b)} \right\rangle \in \mathcal{H}_{P_s}^{(I)} \quad (\text{III.20})$$

b. Variant II

In ETA-Variant II, coarse-grained benchmarking states are prepared using an *adiabatic quantum simulation algorithm* [16]. These algorithms seek to prepare eigenstates of a Hamiltonian [17, 18].

An *initializing Hamiltonian* \hat{H}_i has *known eigenstates* $|\phi_n^{(i)}\rangle$:

$$\hat{H}_i |\phi_n^{(i)}\rangle = \lambda_n^{(i)} |\phi_n^{(i)}\rangle \quad (\text{III.21})$$

The *annealing time* τ parametrizes the *preparation Hamiltonian*:

$$\hat{H}_p^{(i, \tau)}(t) = \left\{ \hat{H}_s - \hat{H}_i \right\} (t/\tau) + \hat{H}_i \quad (\text{III.22})$$

A set of pure states is identified by time-evolving a known eigenstate under preparation Hamiltonians:

$$|\psi_n^{(i, \tau)}\rangle = \hat{U}^{(i, \tau)} |\phi_n^{(i)}\rangle \quad (\text{III.23})$$

$$\hat{U}^{(i, \tau)} = \mathcal{T} \left(e^{-i \int_0^{\tau} dt' \hat{H}_p^{(i, \tau)}(t')} \right) \quad (\text{III.24})$$

The *simulation eigenvalues* $E_n^{(i, \tau)}$ are defined as follows:

$$\hat{H}_s |\alpha_k^s\rangle = \mathcal{E}_{\alpha_k^s} |\alpha_k^s\rangle \quad (\text{III.25})$$

$$\langle \alpha_k^s | \psi_n^{(i, \tau)} \rangle \neq 0, \quad \forall \mathcal{E}_{\alpha_k^s} \in E_n^{(i, \tau)} \quad (\text{III.26})$$

After specifying an initializing Hamiltonian, both the annealing time and the known eigenstate are chosen pseudo-randomly.

The accessible coarse-grained benchmarking states are identified by the parameters (i, τ_b, n_b) for which the following condition holds:

$$E_{n_b}^{(i, \tau_b)} \in \Delta_\epsilon, \quad \forall |\psi_{n_b}^{(i, \tau_b)}\rangle \in \mathcal{H}_{P_s}^{(II)} \quad (\text{III.27})$$

To determine if a coarse-grained benchmarking state was generated, quantum simulation is used to place a bound on the simulation eigenvalues of $|\psi_n^{(i, \tau)}\rangle$.

The *simulated expectation value* is the following:

$$\langle \hat{O}_s(t) \rangle = \langle \psi_n^{(i, \tau)} | e^{i\hat{H}_s t} \hat{O} e^{-i\hat{H}_s t} | \psi_n^{(i, \tau)} \rangle \quad (\text{III.28})$$

$$= \sum_{\alpha^s, \beta^s} c_{\alpha^s}^* c_{\beta^s} \langle \alpha^s | \hat{O} | \beta^s \rangle e^{-it(\mathcal{E}_{\beta^s}^s - \mathcal{E}_{\alpha^s}^s)} \quad (\text{III.29})$$

$$= \sum_{\alpha^s, \beta^s} \mathcal{D}_{\alpha^s, \beta^s} e^{-it(\mathcal{E}_{\beta^s}^s - \mathcal{E}_{\alpha^s}^s)} \quad (\text{III.30})$$

The Fourier transform of the simulated expectation value is the following:

$$\langle \hat{O}_s(\omega) \rangle = \int_{-\infty}^{\infty} dt e^{-i\omega t} \langle \hat{O}_s(t) \rangle \quad (\text{III.31})$$

$$= \sum_{\alpha^s, \beta^s} \mathcal{D}_{\alpha^s, \beta^s} \delta\{\omega - (\mathcal{E}_{\alpha^s}^s - \mathcal{E}_{\beta^s}^s)\} \quad (\text{III.32})$$

$$= \sum_{\alpha^s, \beta^s} \mathcal{D}_{\alpha^s, \beta^s} \delta\{\omega - \Delta_{\alpha^s, \beta^s}^s\} \quad (\text{III.33})$$

The Fourier transform is peaked at the *energy gaps* $(\Delta_{\alpha^s, \beta^s}^s)$ of the simulation eigenvalues. The peaks are discernible if $\langle \alpha^s | \hat{O} | \beta^s \rangle \neq 0$.

The *maximum energy-gap* Δ_{\max}^s can be used to place a bound on the simulation eigenvalues:

$$\langle \hat{H}_s \rangle - \Delta_{\max}^s \leq E_n^{(i, \tau)} \leq \langle \hat{H}_s \rangle + \Delta_{\max}^s \quad (\text{III.34})$$

If the simulation eigenvalue bound falls within the energy-window, a coarse-grained benchmarking state was prepared:

$$\langle \hat{H}_s \rangle \pm \Delta_{\max}^s \in \Delta_\epsilon, \quad |\psi_n^{(i, \tau)}\rangle \in \mathcal{H}_{P_s}^{(II)} \quad (\text{III.35})$$

2. Time-Averaging

In ETA-Variant I and ETA-Variant II, the simulated time-averaged expectation values of the coarse-grained benchmarking states must be estimated.

The simulated expectation value averaged over time t_a is the following:

$$\begin{aligned} \langle \hat{O}_s \rangle_{\text{ave}} &= \frac{1}{t_a} \int_0^{t_a} dt' \langle \hat{O}_s(t') \rangle \\ &= \sum_{\alpha^s, \beta^s} \mathcal{D}_{\alpha^s, \beta^s} \frac{1}{t_a} \int_0^{t_a} dt' e^{it'(\Delta_{\alpha^s, \beta^s}^s)} \end{aligned} \quad (\text{III.36})$$

The simulated time-averaged expectation value is well-approximated when t_a is much larger than the *maximum period*, which is set by the *minimum energy-gap* Δ_{\min}^s :²

$$\begin{aligned} t_a &\gg \frac{2\pi}{\Delta_{\min}^s} > \frac{2\pi}{\Delta_{\max}^s}, \\ \langle \hat{O}_s \rangle_{\text{ave}} &\approx \langle \hat{O}_s \rangle \end{aligned} \quad (\text{III.37})$$

To resolve the dynamics, the simulated expectation value must be sampled faster than the *aliasing time*, which is set by the maximum energy-gap [41–43]:

$$t_{\text{samp}} < \frac{\pi}{\Delta_{\max}^s} \quad (\text{III.38})$$

When $\hat{H}_s \rightarrow \hat{H}$, the maximum energy-gap is upper-bounded by the *energy breadth*:

$$\Delta_B = \mathcal{E}_{\max} - \mathcal{E}_{\min} \quad (\text{III.39})$$

The energy breadth is used to place constraints on the time-averaging parameters:

$$t_{\text{samp}} < \frac{\pi}{\Delta_B} \quad (\text{III.40})$$

$$t_a \gg \frac{2\pi}{\Delta_B} \quad (\text{III.41})$$

IV. NUMERICAL IMPLEMENTATION

To examine their efficacy, both ETA-Variant I and ETA-Variant II are applied to a *Hamiltonian family*.

A. Benchmark Procedure

1. Hamiltonian Family

The Hamiltonian family describes a particle of mass m , with a kinetic term that has a length-scale a :

$$\hat{H}_f(\omega, \lambda) = -\frac{1}{2m} \left[\frac{e^{-i\hat{p}a} - e^{i\hat{p}a}}{2a} \right]^2 + \frac{1}{2} \omega \hat{x}^2 + \lambda \hat{x}^3 \quad (\text{IV.1})$$

² This scaling may be considerably relaxed when the *Eigenstate Thermalization Hypothesis* (ETH) is valid [19–40].

The particle is confined to sites in a periodic lattice:

$$\text{sites} : \{-aN, a(-N+1), \dots, a(N-1), aN\} \quad (\text{IV.2})$$

2. Benchmark Hamiltonians

ETA is used to distinguish members of the Hamiltonian family from one another. 1001-site lattices are used.

The *target Hamiltonian* has a fully quadratic potential:

$$\hat{H} = \hat{H}_f(\omega_0, 0) \quad (\text{IV.3})$$

The *corrupted Hamiltonians* are generated by adjusting the cubic potential:

$$\hat{H}_c(\lambda) = \hat{H}_f(\omega_0, \lambda) \quad (\text{IV.4})$$

The *corruption strength* is the following quantity:

$$\eta = a \frac{\lambda}{\omega_0} \quad (\text{IV.5})$$

3. Energy-Window Selection

The *target energy-range* $\Delta_{\mathcal{E}}$ is defined as follows:

$$\mathcal{E}_{\min} \leq \mathcal{E} \leq \mathcal{E}_{\max}, \quad \forall \mathcal{E} \in \Delta_{\mathcal{E}} \quad (\text{IV.6})$$

Three energy-windows are used during the benchmark:

Low-Range: bottom-15% of the target energy-range

Mid-Range: median-15% of the target energy-range

High-Range: top-15% of the target energy-range

4. Observable Selection

The benchmark observable is the following:

$$\hat{X}_a = |\hat{x}|^{1/3} \quad (\text{IV.7})$$

5. Standardization

To establish a standard of comparison, 10^4 benchmark orthodox mixed states are generated. A *bootstrapping algorithm* is used for statistical analysis [44–46].

6. Arbitration

To establish a simulation diagnostic, 10^4 coarse-grained benchmarking states are generated. A bootstrapping algorithm is used for statistical analysis.

B. Numerical Results

1. Low-Range Window

Variant I: ETA-Variant I positively benchmarks the target Hamiltonian. ETA-Variant I negatively benchmarks 3 out of 5 corrupted Hamiltonians (Figure 5).

Variant II: ETA-Variant II positively benchmarks the target Hamiltonian. ETA-Variant II negatively benchmarks 5 out of 5 corrupted Hamiltonians (Figure 6).

2. Mid-Range Window

Variant I: ETA-Variant I positively benchmarks the target Hamiltonian. ETA-Variant I negatively benchmarks 5 out of 5 corrupted Hamiltonians (Figure 7).

Variant II: ETA-Variant II positively benchmarks the target Hamiltonian. ETA-Variant II negatively benchmarks 5 out of 5 corrupted Hamiltonians (Figure 8).

3. High-Range Window

Variant I: ETA-Variant I positively benchmarks the target Hamiltonian. ETA-Variant I negatively benchmarks 5 out of 5 corrupted Hamiltonians (Figure 9).

Variant II: ETA-Variant II positively benchmarks the target Hamiltonian. ETA-Variant II negatively benchmarks 5 out of 5 corrupted Hamiltonians (Figure 10).

V. APPENDIX: MONTE-CARLO METHODS

Monte-Carlo techniques are a class of algorithms that employ successive random sampling [47]. In particular, *Markov-chain Monte-Carlo methods* approximate sampling from a target probability distribution by recording the output of a stochastic numerical simulation [48–51].

As the simulation time τ_s tends to infinity, the simulated distribution recovers the target distribution. The rate of convergence is independent of dimension: $\sim \mathcal{O}(1/\sqrt{\tau_s})$ [52]. The classical computations required for this work are *tractable* [53], even if quantum simulation is unfeasible due to the Hilbert space dimension [9, 54–58].

VI. ACKNOWLEDGEMENTS

*All of us, like sheep, have strayed away;
we have left God's paths to follow our own.
Yet the Lord laid on Him the sins of us all.*

–Isaiah 53:6

–AMDG–

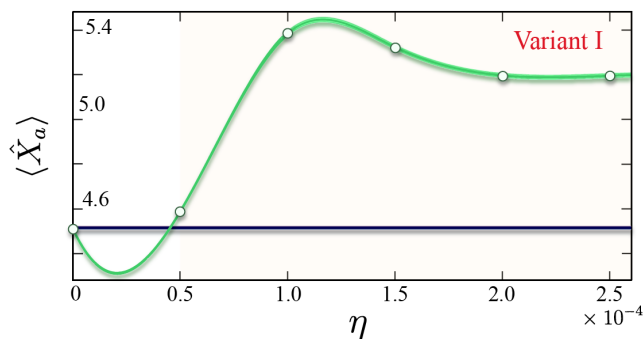


FIG. 5. *Low-Range*: The standard of comparison for the target Hamiltonian is determined using classical computing resources (blue curve). It is contrasted against the simulation diagnostic for the corrupted Hamiltonians (green curve).

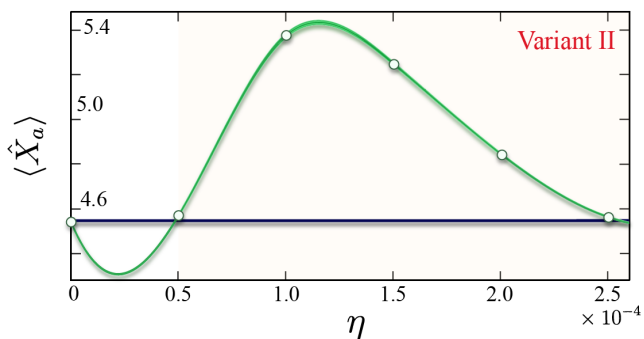


FIG. 6. *Low-Range*: The standard of comparison for the target Hamiltonian is determined using classical computing resources (blue curve). It is contrasted against the simulation diagnostic for the corrupted Hamiltonians (green curve).

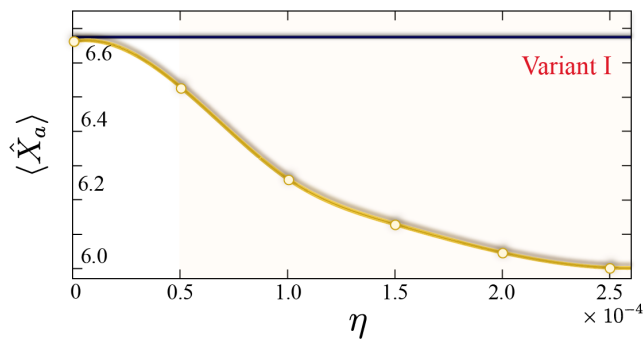


FIG. 7. *Mid-Range*: The standard of comparison for the target Hamiltonian is determined using classical computing resources (blue curve). It is contrasted against the simulation diagnostic for the corrupted Hamiltonians (yellow curve).

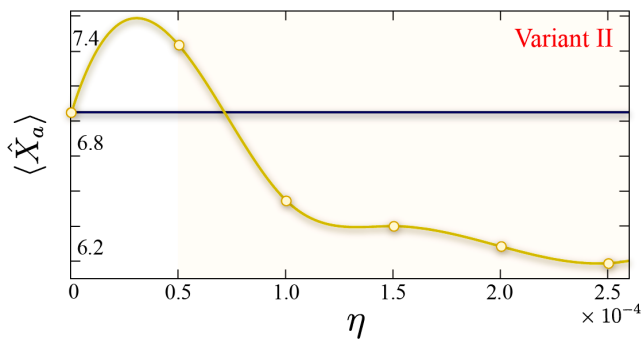


FIG. 8. *Mid-Range*: The standard of comparison for the target Hamiltonian is determined using classical computing resources (blue curve). It is contrasted against the simulation diagnostic for the corrupted Hamiltonians (yellow curve).

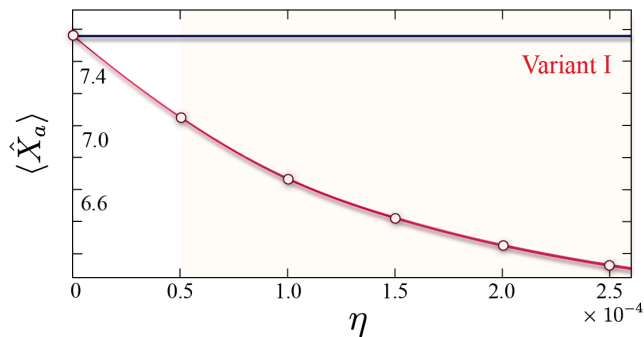


FIG. 9. *High-Range*: The standard of comparison for the target Hamiltonian is determined using classical computing resources (blue curve). It is contrasted against the simulation diagnostic for the corrupted Hamiltonians (red curve).

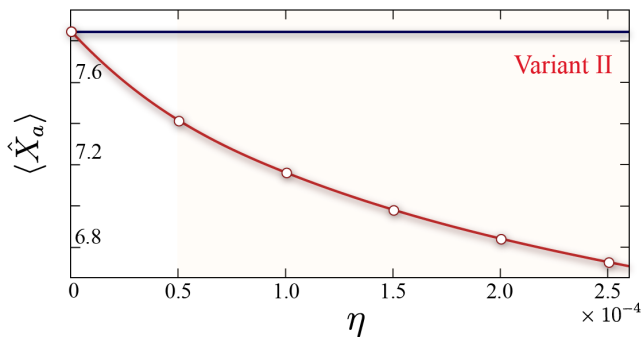


FIG. 10. *High-Range*: The standard of comparison for the target Hamiltonian is determined using classical computing resources (blue curve). It is contrasted against the simulation diagnostic for the corrupted Hamiltonians (red curve).

- [1] E. Schrödinger, Quantization as an eigenvalue problem, *Annalen der Physik* **384**, 361 (1926).
- [2] J. v. Neumann, Probabilistic theory of quantum mechanics, *Nachrichten von der Gesellschaft der Wissenschaften zu Göttingen, Mathematisch-Physikalische Klasse* **1927**, 245 (1927).
- [3] L. Landau, The damping problem in quantum mechanics, in *Collected Papers of L.D. Landau* (Pergamon, 1927) Chap. 2, pp. 8–18.
- [4] M. A. Nielsen and I. L. Chuang, *Quantum computation and quantum information* (Cambridge University Press, 2011) pp. 98–108.
- [5] G. Fubini, On the metrics defined by a hermitian form, *Office graf. C. Ferrari* (1904).
- [6] E. Study, Shortest routes in a complex area, *Mathematische Annalen* **60**, 321 (1905).
- [7] A. Haar, The standard in the theory of continuous groups, *Annals of Mathematics* **34**, 147 (1933).
- [8] L. J. Boya, E. Sudarshan, and T. Tilma, Volumes of compact manifolds, *Reports on Mathematical Physics* **52**, 401 (2003).
- [9] R. P. Feynman, Simulating physics with computers, *International Journal of Theoretical Physics* **21**, 467 (1982).
- [10] Y. I. Manin, Computable and uncomputable, *Sovetskoye Radio, Moscow* (1980).
- [11] A. M. Turing, On computable numbers, with an application to the decision problem, *Proceedings of the London Mathematical Society* **s2-42**, 230 (1937).
- [12] R. P. Feynman, Space-time approach to non-relativistic quantum mechanics, *Rev. Mod. Phys.* **20**, 367 (1948).
- [13] M. A. Nielsen and I. L. Chuang, *Quantum computation and quantum information* (Cambridge University Press, 2011) pp. 70–72.
- [14] A. Peruzzo, J. McClean, P. Shadbolt, M.-H. Yung, X.-Q. Zhou, P. J. Love, A. Aspuru-Guzik, and J. L. O’Brien, A variational eigenvalue solver on a photonic quantum processor, *Nature Communications* **5**, 4213 (2014).
- [15] J. R. McClean, J. Romero, R. Babbush, and A. Aspuru-Guzik, The theory of variational hybrid quantum-classical algorithms, *New Journal of Physics* **18**, 023023 (2016).
- [16] E. Farhi, J. Goldstone, S. Gutmann, and M. Sipser, Quantum Computation by Adiabatic Evolution, arXiv e-prints , quant-ph/0001106 (2000), arXiv:quant-ph/0001106 [quant-ph].
- [17] M. Born and V. Fock, Proof of the adiabatic theorem, *Zeitschrift für Physik* **51**, 165 (1928).
- [18] T. Kato, On the adiabatic theorem of quantum mechanics, *Journal of the Physical Society of Japan* **5**, 435 (1950).
- [19] J. M. Deutsch, Quantum statistical mechanics in a closed system, *Phys. Rev. A* **43**, 2046 (1991).
- [20] M. Srednicki, Chaos and quantum thermalization, *Phys. Rev. E* **50**, 888 (1994).
- [21] M. Rigol, V. Dunjko, and M. Olshanii, Thermalization and its mechanism for generic isolated quantum systems, *Nature* **452**, 854 (2008).
- [22] A. C. Cassidy, C. W. Clark, and M. Rigol, Generalized thermalization in an integrable lattice system, *Phys. Rev. Lett.* **106**, 140405 (2011).
- [23] M. Rigol and M. Srednicki, Alternatives to eigenstate thermalization, *Phys. Rev. Lett.* **108**, 110601 (2012).
- [24] M. P. Müller, E. Adlam, L. Masanes, and N. Wiebe, Thermalization and canonical typicality in translation-invariant quantum lattice systems, *Communications in Mathematical Physics* **340**, 499 (2015).
- [25] S. Xu, X. Li, Y.-T. Hsu, B. Swingle, and S. Das Sarma, Butterfly effect in interacting Aubry-Andre model: Thermalization, slow scrambling, and many-body localization, *Phys. Rev. Research* **1**, 032039 (2019).
- [26] J. Richter, A. Dymarsky, R. Steinigeweg, and J. Gemmer, Eigenstate thermalization hypothesis beyond standard indicators: Emergence of random-matrix behavior at small frequencies, *Phys. Rev. E* **102**, 042127 (2020).
- [27] Y. Kuno, T. Mizoguchi, and Y. Hatsugai, Flat band quantum scar, *Phys. Rev. B* **102**, 241115 (2020).
- [28] A. Schuckert and M. Knap, Probing eigenstate thermalization in quantum simulators via fluctuation-dissipation relations, *Phys. Rev. Research* **2**, 043315 (2020).
- [29] G. Cipolloni, L. Erdős, and D. Schröder, Eigenstate Thermalization Hypothesis for Wigner Matrices, arXiv e-prints , arXiv:2012.13215 (2020), arXiv:2012.13215 [math.PR].
- [30] J. D. Noh, Eigenstate thermalization hypothesis and eigenstate-to-eigenstate fluctuations, *Phys. Rev. E* **103**, 012129 (2021).
- [31] Y. Huang, Finite-size scaling analysis of eigenstate thermalization, arXiv e-prints , arXiv:2103.01539 (2021), arXiv:2103.01539 [cond-mat.stat-mech].
- [32] G. Nakerst and M. Haque, Eigenstate thermalization scaling in approaching the classical limit, *Phys. Rev. E* **103**, 042109 (2021).
- [33] S. M. H. Halataei, On eigenstate thermalization in the SYK chain model, arXiv e-prints , arXiv:2104.05291 (2021), arXiv:2104.05291 [hep-th].
- [34] C. Schönlé, D. Jansen, F. Heidrich-Meisner, and L. Vidmar, Eigenstate thermalization hypothesis through the lens of autocorrelation functions, *Phys. Rev. B* **103**, 235137 (2021).
- [35] F. Fritzsche and T. Prosen, Eigenstate thermalization in dual-unitary quantum circuits: Asymptotics of spectral functions, *Phys. Rev. E* **103**, 062133 (2021), arXiv:2103.11694 [cond-mat.stat-mech].
- [36] V. Balachandran, G. Benenti, G. Casati, and D. Poletti, From ETH to algebraic relaxation of OTOCs in systems with conserved quantities, arXiv e-prints , arXiv:2106.00234 (2021), arXiv:2106.00234 [cond-mat.stat-mech].
- [37] K. S. C. Decker, D. M. Kennes, and C. Karrasch, Many-body localization and the area law in two dimensions, arXiv e-prints , arXiv:2106.12861 (2021), arXiv:2106.12861 [cond-mat.dis-nn].
- [38] G. De Palma and C. Rouzé, Quantum concentration inequalities, arXiv e-prints , arXiv:2106.15819 (2021), arXiv:2106.15819 [quant-ph].
- [39] A. Khudorozhkov, A. Tiwari, C. Chamon, and T. Neupert, Hilbert space fragmentation in a 2D quantum spin system with subsystem symmetries, arXiv e-prints , arXiv:2107.09690 (2021), arXiv:2107.09690 [cond-mat.str-el].
- [40] B. Mukherjee, Z. Cai, and W. V. Liu, Constraint-induced breaking and restoration of ergodicity in spin-1 PXP models, *Physical Review Research* **3**, 033201 (2021), arXiv:2104.00699 [quant-ph].
- [41] E. Whittaker, On the functions which are represented by the expansions of the interpolation-theory, *Proceedings of the Royal Society of Edinburgh* **35**, 181 (1915).
- [42] H. Nyquist, Certain topics in telegraph transmission theory, *Transactions of the American Institute of Electrical Engineers* **47**, 617 (1928).
- [43] C. Shannon, Communication in the presence of noise, *Proceedings of the IRE* **37**, 10 (1949).
- [44] B. Efron, Bootstrap methods: Another look at the jackknife, *Ann. Statist.* **7**, 1 (1979).
- [45] H. R. Kunsch, The jackknife and the bootstrap for general stationary observations, *Ann. Statist.* **17**, 1217 (1989).
- [46] D. N. Politis and J. P. Romano, The stationary bootstrap, *Journal of the American Statistical Association* **89**, 1303 (1994).
- [47] D. P. Kroese, T. Brereton, T. Taimre, and Z. I. Botev, Why the monte carlo method is so important today, *WIREs Computational Statistics* **6**, 386 (2014).
- [48] N. Metropolis, A. W. Rosenbluth, M. N. Rosenbluth, A. H. Teller, and E. Teller, Equation of state calculations by fast computing machines, *The Journal of Chemical Physics* **21**, 1087 (1953).
- [49] W. K. Hastings, Monte Carlo sampling methods using Markov chains and their applications, *Biometrika* **57**, 97 (1970).
- [50] W. R. Gilks and P. Wild, Adaptive rejection sampling for gibbs sampling, *Journal of the Royal Statistical Society. Series C (Applied Statistics)* **41**, 337 (1992).
- [51] S. D. Hill and J. C. Spall, Stationarity and convergence of the metropolis-hastings algorithm: Insights into theoretical aspects, *IEEE Control Systems Magazine* **39**, 56 (2019).
- [52] R. E. Caflisch, Monte carlo and quasi-monte carlo methods, *Acta Numerica* **7**, 1 (1998).
- [53] A. Cobham, The intrinsic computational difficulty of functions, *North-Holland Publishing* , 24 (1965).
- [54] S. Lloyd, Universal quantum simulators, *Science* **273**, 1073 (1996).
- [55] D. Nagaj, Fast universal quantum computation with railroad-switch local Hamiltonians, *Journal of Mathematical Physics* **51**, 062201 (2010), arXiv:0908.4219 [quant-ph].
- [56] D. W. Berry, A. M. Childs, and R. Kothari, Hamiltonian simulation with nearly optimal dependence on all parameters, arXiv e-prints , arXiv:1501.01715 (2015), arXiv:1501.01715 [quant-ph].
- [57] G. Hao Low and I. L. Chuang, Hamiltonian Simulation by Qubitization, arXiv e-prints , arXiv:1610.06546 (2016), arXiv:1610.06546 [quant-ph].
- [58] J. Haah, M. B. Hastings, R. Kothari, and G. Hao Low, Quantum algorithm for simulating real time evolution of lattice Hamiltonians, arXiv e-prints , arXiv:1801.03922 (2018), arXiv:1801.03922 [quant-ph].